Spin-Orbit-Locking Vectorial Metasurface Holography

Zhipeng Yu, Xinyue Gao, Jing Yao, Haoran Li, Yuzhi Shi, Bo Li, Zhenwei Xie, Xiaocong Yuan, Puxiang Lai,* and Qinghua Song**

Z. P. Yu, X. Y. Gao, B. Li, Q. H. Song
Tsinghua Shenzhen International Graduate School
Tsinghua University
Shenzhen, Guangdong, China
E-mail: song.qinghua@sz.tsinghua.edu.cn
Z. P. Yu, J. Yao, H. R. Li, P. X. Lai
Department of Biomedical Engineering
Hong Kong Polytechnic University
Hong Kong SAR, China
E-mail: puxiang.lai@polyu.edu.hk
Z. P. Yu, J. Yao, H. R. Li, P. X. Lai
Hong Kong Polytechnic University Shenzhen Research Institute
Shenzhen, Guangdong, China
Y. Z. Shi
Institute of Precision Optical Engineering
School of Physics Science and Engineering
Tongji University, Shanghai 200092, China
B. Li, Q. H. Song
Suzhou Laboratory
Suzhou 215000, China
Z. W. Xie, X. C. Yuan
Nanophotonics Research Center
Shenzhen Key Laboratory of Micro-scale Optical Information Technology
Institute of Microscale Optoelectronics
Shenzhen University, Shenzhen 518060, Guangdong, China
E-mail: xcyuan@szu.edu.cn
P. X. Lai
Photonics Research Institute
Hong Kong Polytechnic University
Hong Kong SAR, China

Keywords: spin-orbit-locking, total angular momentum, vectorial holography, metasurface

Abstract: Vectorial metasurface holography, allowing for independent control over the amplitude, phase and polarization distribution of holographic images enabled by metasurfaces, plays a crucial role in the realm of optical display, optical and quantum communications. However, previous research on vectorial metasurface holography has typically been restricted to single degree of freedom input and single channel output, thereby demonstrating a very limited modulation capacity. In this work, we present a novel method to achieve multi-channel vectorial metasurface holography by harnessing spin-orbit-locking vortex beams. In each channel, the optical vectorial field is encoded with a pair of total angular momentums (TAMs) featuring two orthogonal spin angular momentums (SAMs) independently locked with arbitrary orbital angular momentums (OAMs). Our methodology relies on a modified Gerchberg-Saxton (GS) algorithm, enabling the encoding of various TAM channels within a single phase profile. Consequently, a pure geometry-phase metasurface with a non-interleaved approach can be used to support such multi-channel vectorial holography, achieving high selectivity of both SAM and OAM, and offering precise routing and manipulation of complex light channels. Our work presents a paradigm shift in the field of holography, offering promising avenues for high-density optical information processing and future photonic device design.

1. Introduction

Vectorial holography[1-4] offers not only control over the amplitude and phase of the holographic image but also the ability to arbitrarily tailor its polarization distribution, which is challenged to be achieved using conventional holographic setup due to the limited degrees of freedom (DoFs)[5]. Metasurfaces, which consist of arrays of 2D subwavelength structures, provide exceptional precision in manipulating the phase, polarization and amplitude of light[6-21]. These properties have made metasurfaces an essential platform for achieving compact, efficient, and adaptable vectorial holography, known as vectorial metasurface holography[22-26]. However, existing studies are typically constrained by offering a single DoF input and a static single-channel output, which significantly limits their modulation capacity.

Orbital angular momentum (OAM) constitutes an additional DoF in optical field[27-30], characterized by the formula $e^{j(l\theta)}$, where $j^2 = -1$, l and θ denote its topological charge (TC) and azimuth angle, respectively. Unlike other optical DoFs, OAM theoretically provides unlimited orthogonal set of helical modes represented by an infinite range of TCs, showcasing significant potentials for enhancing operational channels and information capacity in optical and quantum communications. By exploiting the sampling technique in the holographic algorithms, it becomes feasible to generate OAM holography that can transfer the OAM properties from an incident OAM beam to a holographic image[31-35]. Despite the fact that OAM holography is compatible with other DoFs to enhance multiplexing capabilities, such as spin-selective OAM holography[36] and wavelength-selective OAM holography[37], leveraging the OAM for generating multiplexed vectorial holography remains elusive. It is anticipated that the successful implementation of OAM vectorial holography could lead to substantial advancements in the performance of holographic systems and introducing new DoFs for manipulating vectorial holography.

In this study, we present a novel approach to achieve spin-orbit-locking vectorial metasurface holography (SOL-VMH) by harnessing total angular momentum (TAM) with a value of $|\sigma, l\rangle$ defined as the locking of spin angular momentum (SAM) σ and OAM l. Each channel utilizes a pair of TAMs, corresponding to two orthogonal SAM states, with each state independently locked with an arbitrary OAM, to encode the optical vectorial field. We employ a modified Gerchberg-Saxton (GS) algorithm[3] to calculate the phase profiles of each TAM channel, enabling the generation of vectorial field with independent control over image intensity, polarization azimuth, and ellipticity angles. To accomplish multi-channel vectorial holography, a collective phase profile is derived by summing all the individual phase profiles from each TAM channel. The resulting phase profile for achieving multi-channel vectorial holography can be perfectly supported by a geometry-phase metasurface using a non-interleaved method[38]. Due to the conservation of OAM, and the nature of geometry-phase acting on spin conversion of SAM, only specific pairs of inverse TAMs ($|-\sigma, -l\rangle$) excitation can reconstruct the optical vectorial field in each channel, showcasing exceptional spin-orbit selectivity. The proposed SOL-VMH not only broadens the scope of light manipulation techniques but also demonstrates a high degree of selectivity. This selectivity resulting from the precise control over both SAM and OAM allows for the independent routing and manipulation of different light channels. Our approach, therefore, offers a promising

avenue for the future development of optical and quantum devices requiring sophisticated control and multiplexing capabilities.

2. Results

2.1. Design principle of SOL-VMH.

The schematic of SOL-VMH is illustrated in **Figure 1**. Each input comprises a pair of TAMs ($|\sigma, l\rangle$) defined as the locking of SAM σ and OAM l, where SAM has two states ($\sigma_+ = 1$ and $\sigma_- = -1$, representing left- (LCP) and right-circular polarization (RCP), respectively), and OAM has unbounded and orthogonal set of states with integer TCs. Such a TAM pair can be represented by a matrix $[\sigma_+, l_+; \sigma_-, l_-]$ as shown in Figure 1a, consisting of two orthogonal SAM states ($\sigma_+ = -\sigma_-$), where each SAM state is independently locked with an arbitrary OAM, also known as higher-order Poincare sphere beam[39] as shown in Figure 1b. Notably, the TAMs with different input matrices are orthogonal to each other, laying the foundation for multiplexing vectorial holography on a single metasurface as shown in Figure 1c. Only when the TAM pair with corresponding input matrix is projected onto the metasurface, a specific channel of vectorial holography can be reconstructed, yielding a 2D point-like field distribution with desired amplitude (A), polarization azimuth (ψ) and ellipticity (χ) distributions. For instance, when Input1, represented by matrix [1, 1; -1, 2], is illuminated onto the metasurface, only the vectorial field encoded in Output1 can be distinctly recognized and retrieved, revealing clear details of three images across three optical dimensions: amplitude, polarization azimuth, and ellipticity angle.

2.2. Algorithm development and simulated results.

The methodology of SOL-VMH is illustrated in **Figure 2a**. Each modulated vectorial field (U^i) in channel i is obtained by multiplying the original vectorial field with a 2D Dirac comb function (C^i with a constant period of d). Notably, each channel is positioned at distinct spatial locations across the optical field, with the full configuration not shown in Figure 2a for better visualization and detailed arrangement of the vector fields can be found in Supplementary Note 1. The value of d can be arbitrarily chosen as long as the point-like field remains discernible. In each TAM channel, two desired phases ($\varphi^i_{\sigma_\pm}$) corresponding to opposite SAM states are calculated from the previous modulated vectorial field in the spatial frequency domain using a modified GS algorithm[3] (see more details in Supplementary Note 2). An arbitrary OAM helical phase ($\phi^i_{l_\pm}$) is then superimposed with

$\varphi_{\sigma_\pm}^i$ to achieve the purpose of spin-orbit-locking. Subsequently, the superimposed phase associated with the σ_+ SAM state is inverted due to the opposite sign of geometry-phase for the two SAM states. As a result, the final phase profile supporting all channels can be expressed as,

$$\varphi_{SOL-VMH} = arg\left[\sum_{i=1}^{N}\left(e^{j\left(\varphi_{\sigma_-}^i+\phi_{l_-}^i\right)}+e^{j\left(-\varphi_{\sigma_+}^i-\phi_{l_+}^i\right)}\right)\right] \quad (1)$$

where channel i = 1, 2,…, N, with N being the total number of channels, $\phi_{l_-}^i$ and $\phi_{l_+}^i$ are the helical phases corresponding to TCs of OAM l_-^i and l_+^i, respectively, which are added into the calculated phases $\varphi_{\sigma_-}^i$ and $\varphi_{\sigma_+}^i$ for their respective SAM states.

This metasurface comprises an array of elliptical titanium dioxide (TiO_2) meta-pillars on a glass (SiO_2) substrate, each with 600 nm in height and arranged in a square lattice with a periodicity of 300 nm. These meta-pillars are designed as half-wave plates with axis lengths of 100 nm and 260 nm, enabling them to convert the spin of circularly polarized (CP) beams. The rotation of the meta-pillar, determined by angle δ, facilitates this CP conversion: $|\sigma_+\rangle \rightarrow e^{j2\delta}|\sigma_-\rangle$ and $|\sigma_-\rangle \rightarrow e^{-j2\delta}|\sigma_+\rangle$, *i.e.*, the beams are converted to the opposite spin with a geometry-phase (or Pancharatnam-Berry (PB) phase) of 2δ and -2δ, respectively. Consequently, the two-dimensional rotation angle profile (φ_δ) of the metasurface can be derived as,

$$\varphi_\delta = \frac{1}{2}(\varphi_{SOL-VMH} - \beta) \quad (2)$$

where β is the propagation phase of the meta-pillar, which is constant for all meta-pillars due to their uniform sizes. For simplicity, we ignore the propagation phase and set it as $\beta = 0°$. Therefore, by rotating the meta-pillars, a pure geometry-phase can be obtained. The phase profile derived from the aforementioned process can be encoded in a geometry-phase metasurface using a non-interleaved method[38]. When illuminated by incident waves possessing both σ_+ and σ_- SAM, the metasurface generates a symmetric pair of diffracted beams as shown in Figure 2b, allowing for precise control over amplitude and polarization by superimposing both SAM states. In the i^{th} channel, the optical vectorial field is encoded with a TAM pair $[\sigma_-, l_-^i; \sigma_+, l_+^i]$. To reconstruct the vectorial holographic images from the metasurface, an inverse TAM pair $[\sigma_+, -l_-^i; \sigma_-, -l_+^i]$ with opposite sign of SAM and OAM is used for illumination due to the conservation of OAM and the cross-polarization conversion of SAM. When illuminating with a vortex beam carrying TAM $|\sigma_+, -l_-^i\rangle$ onto the metasurface (Figure 2b(I)), the output optical field $F_{\sigma_-}(\varphi_{\sigma_-}^i)$ in the Fourier plane on the left side corresponds to the σ_- component of the desired vectorial field, where F represents the

Fourier transform. Similarly, illuminating a vortex beam with TAM $|\sigma_-, -l_+^i\rangle$ (Figure 2b(II)) yields the output optical field $F_+(\varphi_{\sigma_+}^i)$ on the left constituting the σ_+ component. Due to the opposite response of the geometry-phase on the two CP beams, conjugate vectorial holographic images are produced on the right side, which are beyond the scope and thus ignored in the following discussions. Finally, by illuminating an incident beam possessing the TAM pair of $[\sigma_+, -l_-^i; \sigma_-, -l_+^i]$, the desired vectorial field can be reconstructed on the left side (Figure 2b(III)).

Remarkably, our approach enables theoretically unlimited channels for SOL-VMH. As a proof of concept, we demonstrate simulation results with four channels as an example. As depicted in Figure 2a, we employ four optical vectorial fields, each encoded with three binary patterns representing amplitude ($A = 0.5, 0.866$), azimuth angle ($\psi = -45°, 45°$), and ellipticity angle ($\chi = -22.5°, 22.5°$). The four encoded TAM pairs are [-1, -12; 1, 11], [-1, 10; 1, -7], [-1, 8; 1, 9], and [-1, -16; 1, 5]. Therefore, four inverse TAM pairs of [1, 12; -1, -11], [1, -10; -1, 7], [1, -8; -1, -9], and [1, 16; -1, -5] are utilized as the incident light to reconstruct the desired vectorial fields as shown in **Figure 3(I)**. The resulting amplitude profiles are shown in Figure 3(II), exhibiting point-like distributions with designed patterns of "triangle", "square", "circle", and "heart" shapes. The corresponding polarizations of the output fields are further analyzed. Figures 3(III) and 3(IV) illustrate the azimuth angle distributions of "fish", "snail", "octopus", and "rabbit", and the ellipticity angle distributions of "starfish", "butterfly", "Mickey", and "turtle" in each channel, respectively, corresponding to the intentionally designed patterns in Figure 2a. Detailed results can be referred to Supplementary Note 3). It can be observed that in the designated corresponding channel, the correct beam incident will cause the corresponding spot array pattern to emerge, allowing for the further identification of polarization without considering the crosstalk. A detailed analysis of the crosstalk is provided in Supplementary Note 4.

2.3. Experimental results with identical OAMs in each TAM channel ($l_+^i = l_-^i$)

In the following experiment, we concentrated on encoding the polarization state of the optical vectorial field with a uniform intensity distribution to ensure optimal experimental polarization outcomes. The footprint of metasurface supporting the SOL-VMH is 240 μm × 240 μm consisting of 800 × 800 pixels of nano-pillars. Scanning electron microscope (SEM) images depicting the top and perspective view of the

fabricated metasurface are presented in **Figure 4a** (see more fabrication details in Methods section). The experimental schematic diagram is shown in Figure 4b (see more details in Methods section).

We first demonstrate identical OAM in each TAM pair, i.e., $l_+^i = l_-^i$. As a proof of concept, we utilized two TAM channels (N = 2) for the multiplexing, encoded with TAM pairs of [-1, 2; 1, 2] and [-1, 1; 1, 1]. In this scenario, each TAM pair degenerates into a linearly polarized vector beam with a single OAM. Therefore, the experimental conditions can be simplified, and vortex beams with TC of -2 or -1 in the horizontal polarization are illuminated onto the metasurface to reconstruct the desired vectorial fields. In Figure 4b, the first quarter-wave plate (QWP1) and one of the spatial light modulators (SLM2) in red dashed boxes are blocked. As depicted in Figures 4c(I) and 4d(I), upon illuminating vector beams with TCs of -2 and -1 in horizontal polarization, point-like intensity distributions are observed in the corresponding regions. In contrast, donut-shaped intensity distributions are observed when there is a TAM mismatch between input and output, as shown in Figures 4c,d(IV). To assess the polarization properties, a polarizer is placed before the camera for analysis. Unlike previous studies of OAM multiplexed holography that utilize a fundamental mode filtering aperture array for post processing[31], in order to better reproduce the experimental results, we present the original measured optical images in the following discussions. Figures 4c,d(II) and (III) present the measured intensity profiles with the polarizer oriented at 0° and 90°, respectively, revealing complementary patterns due to the orthogonality of horizontal and vertical polarizations. The polarization ellipticity and azimuth angle distributions of the vectorial fields are determined via Stokes parameter measurements (see more details in Supplementary Note 5). The reconstructed patterns in channel 1, depicting a “deer” and a “bird”, and in channel 2, depicting a “fish” and a “bat”, shown in the second row of Figures 4e and 4f, respectively, closely match the target images displayed in the first row. More experimental results of more channels can be referred to Supplementary Note 6.

2.4. Experimental results with distinct OAMs in each TAM channel ($l_+^i \neq l_-^i$)

We proceed to demonstrate distinct OAMs in each TAM pair channel, i.e., $l_+^i \neq l_-^i$. Specifically, two channels are encoded with TAM pairs of [-1, 3; 1, 4] and [-1, 1; 1, 2], respectively, each carrying different OAMs. The optical setup is shown in Figure 4b, where a half-wave plate is employed to adjust the ratio of optical intensities reflected by two SLMs, ensuring equivalent intensities within each TAM pair. Two sets of input

fields with each carrying a pair of TAMs, denoted as [1, -3; -1, -4] and [1, -1; -1, -2], are used to reconstruct the optical vectorial fields, resulting in point-like intensity distributions in the corresponding areas without putting any optical analyzer as shown in **Figures 5a,b(I)**. Figures 5a,b(II) and (III) display the optical output intensity distributions under two opposite SAM states, revealing complementary patterns due to the orthogonality of these two states. For a more direct comparison, the vectorial images designed in this experiment are identical to those in the preceding experiment shown in Figure 4. The reconstructed azimuth and ellipticity angle patterns for channel 1 (a "deer" and a "bird") and channel 2 (a "fish" and a "bat"), as displayed in Figures 5a,b(IV) and (V), exhibit a strong agreement with their respective target images presented in the first row of Figures 4e and 4f. To furtherly validate the robustness of the selectivity, vortex beams with various TCs ranging from 0 to -4 in horizontal polarization are projected onto the metasurface. The corresponding intensity distributions within the designed channels are illustrated in Figures 5c and 5d. Each of these images exhibits two types of donut patterns or their superimposed structures, which showcases the supposition of a pair of spin-orbit-locking holographic fields, thus underscoring high reliability and security of the proposed approach.

3. Discussion

We have successfully implemented spin-orbit-locking multi-channel vectorial metasurface holography using TAM as the input. Our approach allows for a pair of desired TAMs serving as the input to project onto a geometry-phase metasurface for the reconstruction of the corresponding optical vectorial field. This field exhibits a 2D point-like intensity distribution with designed profile of amplitude, polarization azimuth and ellipticity angles. The system demonstrates high selectivity, effectively preventing the acquisition of the optical vectorial field in case of incorrect inputs or mismatches between input and output. Only binary values for amplitude, azimuth, and ellipticity angles are presented to enhance visualization in this work. However, it's important to note that these three parameters can take any arbitrary value, as they can be independently adjusted.

In this study, a geometry-phase metasurface consisting of TiO_2 nanopillars exhibits an inherent broadband response of intensity and polarization in the visible range, ensuring robust performance across this range[6]. The use of the geometric phase in a single unit cell with identical structures allows for high tolerance to fabrication errors

in the metasurface. This results in holographic images deviating from the incident direction[40]. With improved fabrication techniques, more solutions can be introduced. The combination of geometric phase and propagation phase also enables the independent design of the required phase profiles for both spin states using the GS algorithm[41]. Furthermore, a supercell metasurface can bypass the GS algorithm and instead use the faster Fourier transform algorithm directly[42].

The spin-orbit-locking phenomena can significantly enhance the hologram's capacity and security. This is due to the OAM, which theoretically provides an unlimited set of orthogonal helical modes represented by an extensive range of TCs. Additionally, the distinct OAMs in each TAM pair lead to asymmetric responses in the two orthogonal spin states. Combined with advanced techniques such as electrically tunable metamaterials and nonlinear optical responses, this feature can further enhance the application potential, particularly in the realms of optical encryption and video recording[31, 43, 44]. Moreover, integration with other DoFs, such as wavelength, is feasible by introducing varied meta-pillar structures[37]. The optical vectorial field in each channel can be further selectively positioned in different planes for generating three-dimensional SOL-VMH by incorporating an Fourier transform (FT) lens with chosen focal lengths[31] (see more details of numerical demonstration in Supplementary Note 7). Such a feature can enhance the integration density of the device, thereby providing more information with greater DoFs for broader applications such as OAM-selected virtual/augmented reality (VR/AR) and OAM-selected light detection and range (LiDAR)[45]. So far, the fabrication of metasurfaces is relatively expensive, making large-scale production challenging. In the future, improvements in manufacturing processes[46-48], including DUV lithography and nanoimprint lithography, as well as the development of more efficient materials applicable to various wavelength bands, will lead to cost-effective mass production of metasurfaces. This will greatly unleash the application potential of metasurfaces.

Overall, the development of SOL-VMH enables the simultaneous and independent control of SAM and OAM, introduces multiple degrees of selectivity due to the spin-orbit-locking feature. This advancement holds promise to revolutionize optics by offering locally controlled complex optical fields through various TAM pairs. The increased capacity and security in optical communication systems achieved through such precise control could enhance the information encoding reliability. Furthermore, the intricate manipulation of polarization, phase, and intensity paves the way for enhanced interactions with other research fields, such as quantum computing and optical force

manipulation, where the control and manipulation of light at such granular levels are paramount.

Methods

Sample fabrication

The metasurface fabrication process involves electron beam lithography (EBL) and reactive ion etching (RIE) techniques. Initially, a 600-nm-thick titanium dioxide (TiO_2) film is deposited on a polished glass (SiO_2) substrate via electron beam evaporation (EBE). A polymethyl methacrylate (PMMA) layer is then spin-coated onto the TiO_2 film. After EBL, the PMMA resist is developed, and a chromium (Cr) film is deposited onto the patterned PMMA using EBE. The unexposed PMMA is removed, and the TiO_2 is etched using RIE. The process concludes with the removal of the Cr mask through chemical etching.

Optical setup

The experimental schematic diagram for the vectorial holography is Fig. 3b. A collimated continuous-wave coherent laser beam with a wavelength of 488nm (OBIS, Coherent, USA) is first polarized by a half wave plate (HWP) and then directed onto a beam splitter (BS), which divides it into two distinct beams. Each beam is then projected perpendicularly onto a spatial light modulator (SLM, HOLOEYE PLUTO VIS056, German). A polarizer (P1) with horizontal polarization is placed in front of one SLM (SLM1), and the other polarizer (P2) with the vertical polarization is placed in front of the remaining SLM (SLM2), enabling the modulation of these two beams with orthogonally linear polarizations. These two beams are modulated and reflected by SLMs and reunified into a single beam at the original BS. A quarter-wave plate (QWP1) is positioned behind the beam splitter (BS) to transform horizontally polarized light into a SAM state of σ- and vertically polarized light into a SAM state of σ+. Then it is slightly focused on the metasurface using a lens (L1, f = 50 mm) to generate optical vector field. An aspheric lens (L2, f = 16 mm) with a numerical aperture (NA) of 0.65 is placed behind the metasurface to execute a Fourier transform on the optical field in the metasurface plane. The optical field in the focal plane of L2 is transmitted to a scientific CMOS (sCMOS) camera (Dhyana 400BSI V2, Tucsen, China) via a 4-f system, which includes a pair of lenses (L3 and L4, not shown in the figure for simplicity). To analyze the polarization state of the optical field, another QWP (QWP2) and a polarizer (P3) are strategically positioned in front of the sCMOS camera.

Supporting Information

Supporting Information is available from the Wiley Online Library or from the author.

Acknowledgements

Q.S. acknowledges the funding support from the National Natural Science Foundation of China (12204264), the Jiangsu Provincial Fundamental Research Program (BK20243029), the Shenzhen Science and Technology Innovation Commission (JCYJ20230807111706014); P.L. acknowledges the funding support from the National Natural Science Foundation of China (81930048), the Guangdong Science and Technology Commission (2019BT02X105), Hong Kong Research Grant Council (15217721, 15125724, C7074-21), the Shenzhen Science and Technology Innovation Commission (JCYJ20220818100202005), and the Hong Kong Polytechnic University (P0045680, P0043485, P0045762, P0049101).

Received: ((will be filled in by the editorial staff))
Revised: ((will be filled in by the editorial staff))
Published online: ((will be filled in by the editorial staff))

References

[1] Z.-L. Deng, Z.-Q. Wang, F.-J. Li, M.-X. Hu, X. Li, *Nanophotonics* **2022**, 11, 1725.
[2] Q. Song, X. Liu, C.-W. Qiu, P. Genevet, *Appl. Phys. Rev.* **2022**, 9, 011311.
[3] Q. Song, A. Baroni, P. C. Wu, S. Chenot, V. Brandli, S. Vezian, B. Damilano, P. de Mierry, S. Khadir, P. Ferrand, P. Genevet, *Nat. Commun.* **2021**, 12, 3631.
[4] Z. Yang, P.-S. Huang, Y.-T. Lin, H. Qin, J. Zúñiga-Pérez, Y. Shi, Z. Wang, X. Cheng, M.-C. Tang, S. Han, *Nat. Commun.* **2024**, 15, 232.
[5] T. Todorov, L. Nikolova, N. Tomova, *Appl. Optics* **1984**, 23, 4309.
[6] Q. Song, A. Baroni, R. Sawant, P. Ni, V. Brandli, S. Chenot, S. Vezian, B. Damilano, P. de Mierry, S. Khadir, P. Ferrand, P. Genevet, *Nat. Commun.* **2020**, 11, 2651.
[7] J. P. Balthasar Mueller, N. A. Rubin, R. C. Devlin, B. Groever, F. Capasso, *Phys. Rev. Lett.* **2017**, 118, 113901.
[8] M. Liu, W. Zhu, P. Huo, L. Feng, M. Song, C. Zhang, L. Chen, H. J. Lezec, Y. Lu, A. Agrawal, *Light Sci. Appl.* **2021**, 10, 107.
[9] Q. Song, M. Odeh, J. Zúñiga-Pérez, B. Kanté, P. Genevet, *Science* **2021**, 373, 1133.
[10] A. C. Overvig, S. Shrestha, S. C. Malek, M. Lu, A. Stein, C. Zheng, N. Yu, *Light Sci. Appl.* **2019**, 8, 92.
[11] B. Xiong, Y. Liu, Y. Xu, L. Deng, C.-W. Chen, J.-N. Wang, R. Peng, Y. Lai, Y. Liu, M. Wang, *Science* **2023**, 379, 294.
[12] Z. L. Deng, Q. A. Tu, Y. Wang, Z. Q. Wang, T. Shi, Z. Feng, X. C. Qiao, G. P. Wang, S. Xiao, X. Li, *Adv. Mater.* **2021**, 33, 2103472.
[13] S. So, J. Kim, T. Badloe, C. Lee, Y. Yang, H. Kang, J. Rho, *Adv. Mater.* **2023**, 35, 2208520.
[14] T. Naeem, J. Kim, H. S. Khaliq, J. Seong, M. T. S. Chani, T. Tauqeer, M. Q. Mehmood, Y. Massoud, J. Rho, *Adv. Opt. Mater.* **2023**, 11, 2202278.

[15] P. Georgi, Q. Wei, B. Sain, C. Schlickriede, Y. Wang, L. Huang, T. Zentgraf, *Sci. Adv.* **2021**, 7, eabf9718.
[16] S. Latif, J. Kim, H. S. Khaliq, N. Mahmood, M. A. Ansari, X. Chen, J. Akbar, T. Badloe, M. Zubair, Y. Massoud, *Nano Lett.* **2024**, 24, 708.
[17] H. Zhou, B. Sain, Y. Wang, C. Schlickriede, R. Zhao, X. Zhang, Q. Wei, X. Li, L. Huang, T. Zentgraf, *ACS Nano* **2020**, 14, 5553.
[18] Z. Yu, H. Li, W. Zhao, P.-S. Huang, Y.-T. Lin, J. Yao, W. Li, Q. Zhao, P. C. Wu, B. Li, *Nat. Commun.* **2024**, 15, 2607.
[19] S. A. Schulz, R. Oulton, M. Kenney, A. Alù, I. Staude, A. Bashiri, Z. Fedorova, R. Kolkowski, A. F. Koenderink, X. Xiao, *Appl. Phys. Lett.* **2024**, 124.
[20] Q. Song, S. Khadir, S. Vézian, B. Damilano, P. de Mierry, S. Chenot, V. Brandli, R. Laberdesque, B. Wattellier, P. Genevet, *Nanophotonics* **2020**, 10, 697.
[21] Z. Yang, P.-S. Huang, Y.-T. Lin, H. Qin, J. Chen, S. Han, W. Huang, Z.-L. Deng, B. Li, J. Zúñiga-Pérez, *Nano letters* **2024**, 24, 844.
[22] S. Zhang, L. Huang, X. Li, R. Zhao, Q. Wei, H. Zhou, Q. Jiang, G. Geng, J. Li, X. Li, *Acs Photonics* **2021**, 8, 1746.
[23] D. Wang, F. Liu, T. Liu, S. Sun, Q. He, L. Zhou, *Light Sci. Appl.* **2021**, 10, 67.
[24] Z.-L. Deng, J. Deng, X. Zhuang, S. Wang, K. Li, Y. Wang, Y. Chi, X. Ye, J. Xu, G. P. Wang, *Nano Lett.* **2018**, 18, 2885.
[25] N. Mao, G. Zhang, Y. Tang, Y. Li, Z. Hu, X. Zhang, K. Li, K. Cheah, G. Li, *Proc. Natl. Acad. Sci. U. S. A.* **2022**, 119, e2204418119.
[26] Z. L. Deng, M. Jin, X. Ye, S. Wang, T. Shi, J. Deng, N. Mao, Y. Cao, B. O. Guan, A. Alù, *Adv. Funct. Mater.* **2020**, 30, 1910610.
[27] Y. Shen, X. Wang, Z. Xie, C. Min, X. Fu, Q. Liu, M. Gong, X. Yuan, *Light Sci. Appl.* **2019**, 8, 90.
[28] L. Allen, M. W. Beijersbergen, R. J. Spreeuw, J. P. Woerdman, *Phys. Rev. A.* **1992**, 45, 8185.
[29] A. M. Yao, M. J. Padgett, *Adv. Opt. Photonics* **2011**, 3, 161.
[30] A. H. Dorrah, N. A. Rubin, M. Tamagnone, A. Zaidi, F. Capasso, *Nat. Commun.* **2021**, 12, 6249.
[31] H. Ren, X. Fang, J. Jang, J. Bürger, J. Rho, S. A. Maier, *Nat. Nanotechnol.* **2020**, 15, 948.
[32] H. Ren, G. Briere, X. Fang, P. Ni, R. Sawant, S. Héron, S. Chenot, S. Vézian, B. Damilano, V. Brändli, S. A. Maier, P. Genevet, *Nat. Commun.* **2019**, 10, 2986.
[33] X. Fang, H. Ren, M. Gu, *Nat. Photonics* **2020**, 14, 102.
[34] Z. Shi, Z. Wan, Z. Zhan, K. Liu, Q. Liu, X. Fu, *Nat. Commun.* **2023**, 14, 1869.
[35] L.-J. Kong, Y. Sun, F. Zhang, J. Zhang, X. Zhang, *Phys. Rev. Lett.* **2023**, 130, 053602.
[36] H. Yang, P. He, K. Ou, Y. Hu, Y. Jiang, X. Ou, H. Jia, Z. Xie, X. Yuan, H. Duan, *Light Sci. Appl.* **2023**, 12, 79.
[37] G. He, Y. Zheng, C. Zhou, S. Li, Z. Shi, Y. Deng, Z.-K. Zhou, *Light Sci. Appl.* **2024**, 13, 98.
[38] Z. H. Jiang, L. Kang, T. Yue, H. X. Xu, Y. Yang, Z. Jin, C. Yu, W. Hong, D. H. Werner, C. W. Qiu, *Adv. Mater.* **2020**, 32, 1903983.
[39] G. Milione, H. Sztul, D. Nolan, R. Alfano, *Phys. Rev. lett.* **2011**, 107, 053601.
[40] X. Zhang, S. Yang, W. Yue, Q. Xu, C. Tian, X. Zhang, E. Plum, S. Zhang, J. Han, W. Zhang, *Optica* **2019**, 6, 1190.
[41] Y. Xu, H. Zhang, Q. Li, X. Zhang, Q. Xu, W. Zhang, C. Hu, X. Zhang, J. Han, W. Zhang, *Nanophotonics* **2020**, 9, 3393.
[42] T. Wu, Q. Xu, X. Zhang, Y. Xu, X. Chen, X. Feng, L. Niu, F. Huang, J. Han, W. Zhang, *Adv. Sci.* **2022**, 9, 2204664.

[43] I. Kim, J. Jang, G. Kim, J. Lee, T. Badloe, J. Mun, J. Rho, *Nat. commun.* **2021**, 12, 3614.
[44] C. Jung, G. Kim, M. Jeong, J. Jang, Z. Dong, T. Badloe, J. K. Yang, J. Rho, *Chem. Rev.* **2021**, 121, 13013.
[45] Y. Yang, J. Seong, M. Choi, J. Park, G. Kim, H. Kim, J. Jeong, C. Jung, J. Kim, G. Jeon, K.-i. Lee, D. H. Yoon, J. Rho, *Light Sci. Appl.* **2023**, 12, 152.
[46] J. Seong, Y. Jeon, Y. Yang, T. Badloe, J. Rho, *Int. J. Pr. Eng. Man-GT* **2024**, 11, 685.
[47] Y. Yang, H. Kang, C. Jung, J. Seong, N. Jeon, J. Kim, D. K. Oh, J. Park, H. Kim, J. Rho, *ACS Photonics* **2023**, 10, 307.
[48] H. Kang, D. Lee, Y. Yang, D. Kyo Oh, J. Seong, J. Kim, N. Jeon, D. Kang, J. Rho, *Photon. Insights* **2023**, 2, R04.

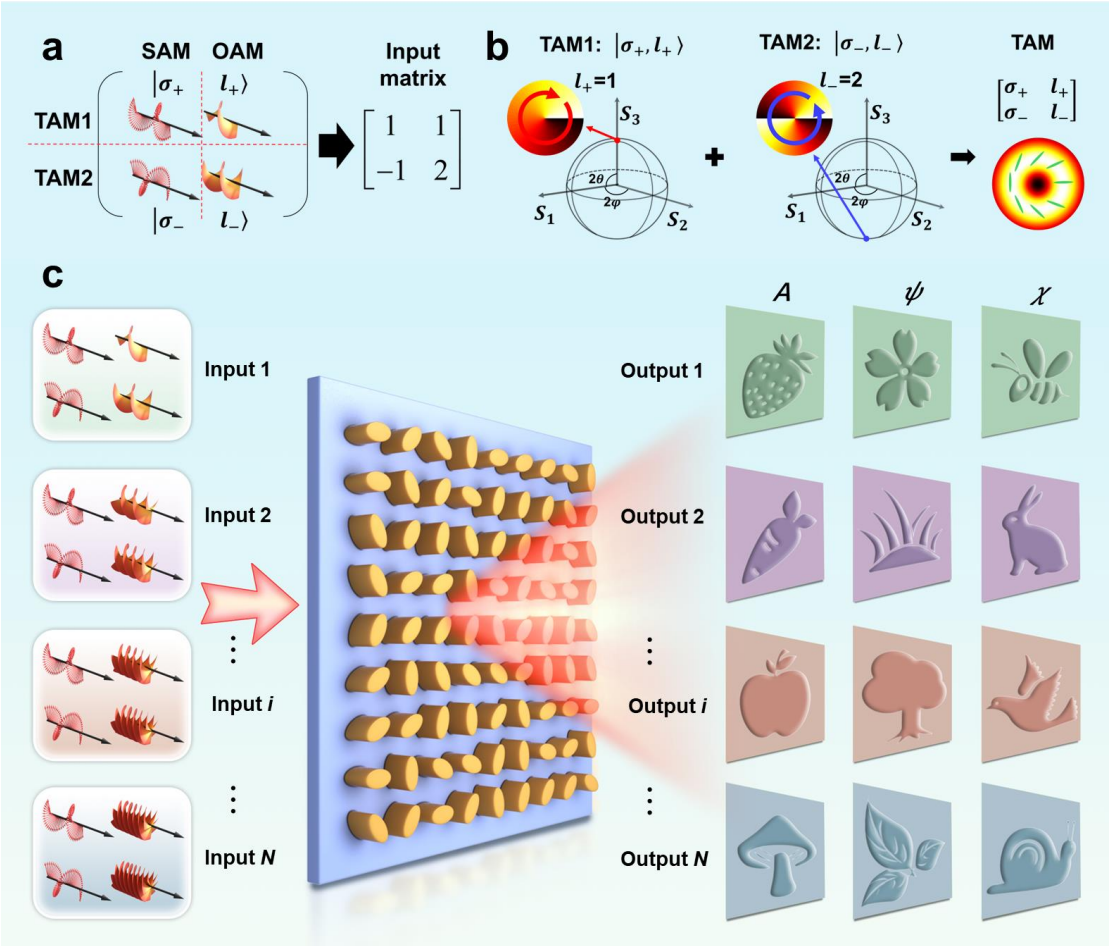

Figure 1. Schematic illustration of the SOL-VMH. (**a**) In each channel, the SOL-VMH is achieved by illuminating a desired input composed with a pair of TAMs (TAM1 and TAM2) that consist of orthogonal SAM states with each independently locked by an arbitrary OAM. The input can be simplified as $[\sigma_+, l_+; \sigma_-, l_-]$. (**b**) TAM1 and TAM2 can be represented as two higher-order Poincare sphere beams. The superposition of them gives rise to a vectorial vortex beam with modulated polarization distribution. (**c**) The metasurface can be multiplexed with various channels of SOL-VMH. In each channel, the reconstructed vectorial field is characterized by desired amplitude (A), polarization azimuth (ψ) and ellipticity (χ) distributions.

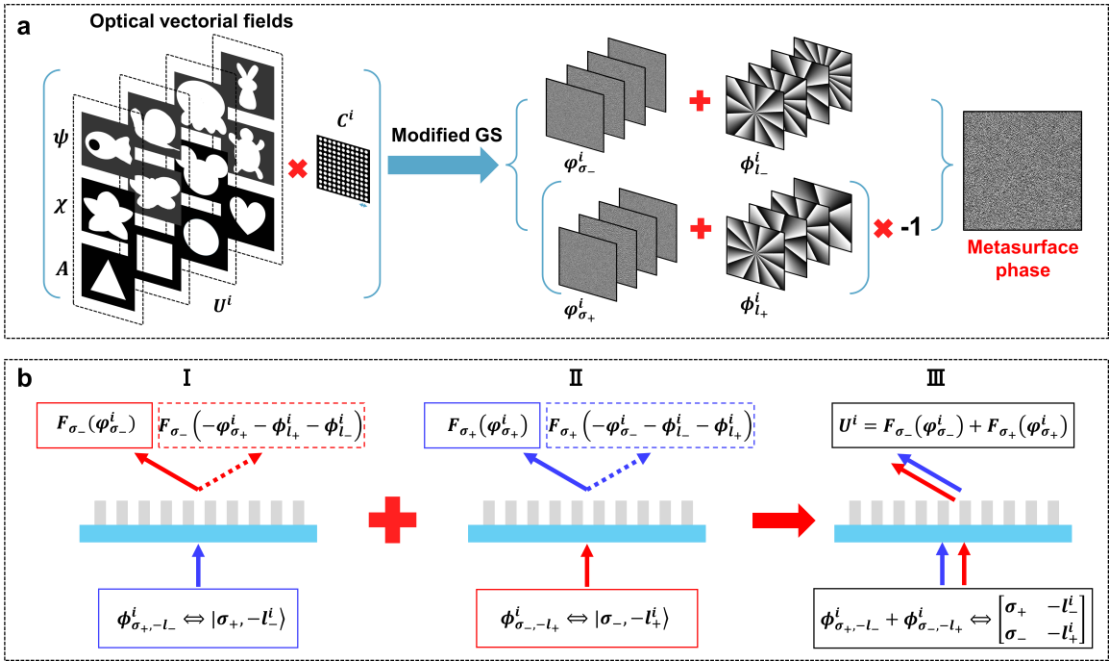

Figure 2. Flowchart and design principle of the SOL-VMH. (**a**) The flowchart for the design of four-channel SOL-VMH. In each channel, the optical vectorial field is encoded with three binary patterns of amplitude (A), azimuth angle (ψ) and ellipticity angle (χ) distributions. This field is then multiplied by a 2D Dirac comb function positioned at distinct spatial locations across the optical field. Subsequently, a modified GS algorithm is employed to extract a pair of phases in two opposite SAM states. The obtained phase is added with the corresponding OAM helical phase. The phase added in σ_+ SAM state is further inverted. This yields a pair of processed phases in two opposite SAM states, forming the hologram for each channel. The final phase profile is superimposed by all holographic channels, leading to the design of multi-channel SOL-VMH. (**b**) The demonstration of a geometry-phase metasurface supporting the SOL-VMH with a non-interleaved method in each channel. F represents the Fourier transform.

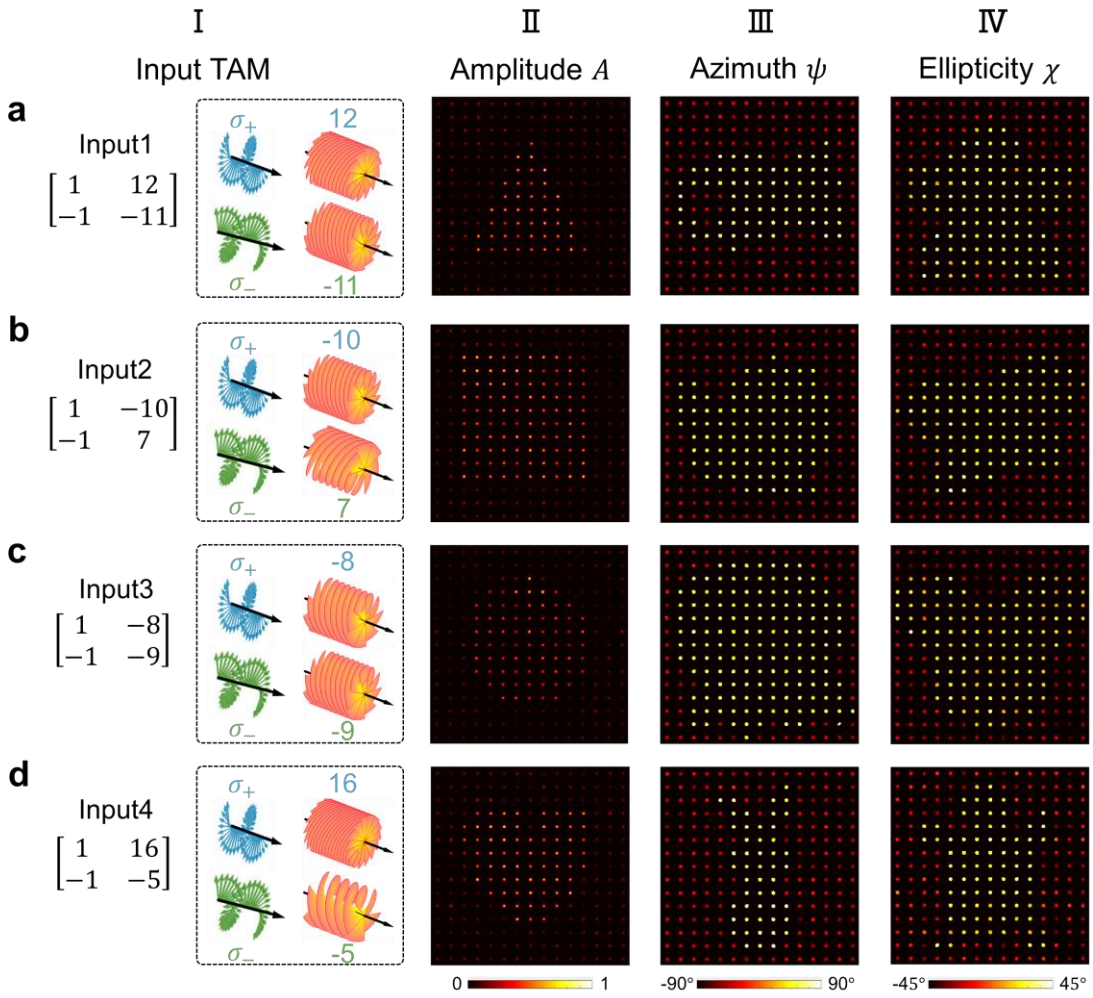

Figure 3. Numerical demonstration of four-channel SOL-VMH with four sets of TAM pairs. The four encoded TAM pairs are [-1, -12; 1, 11], [-1, 10; 1, -7], [-1, 8; 1, 9], and [-1, -16; 1, 5]. Therefore, four inverse TAM pairs of (**a**) [1, 12; -1, -11], (**b**) [1, -10; -1, 7], (**c**) [1, -8; -1, -9], and (**d**) [1, 16; -1, -5] are utilized as the incident light to reconstruct the desired vectorial fields. Column I show the input matrices. The images employed for the amplitude design are “triangle”, “square”, “circle”, and “heart” shapes as shown in column II. The images employed for the polarization azimuth design are “fish”, “snail”, “octopus”, and “rabbit” as shown in column III. The images employed for the polarization ellipticity design are “starfish”, “butterfly”, “Mickey”, and “turtle”.

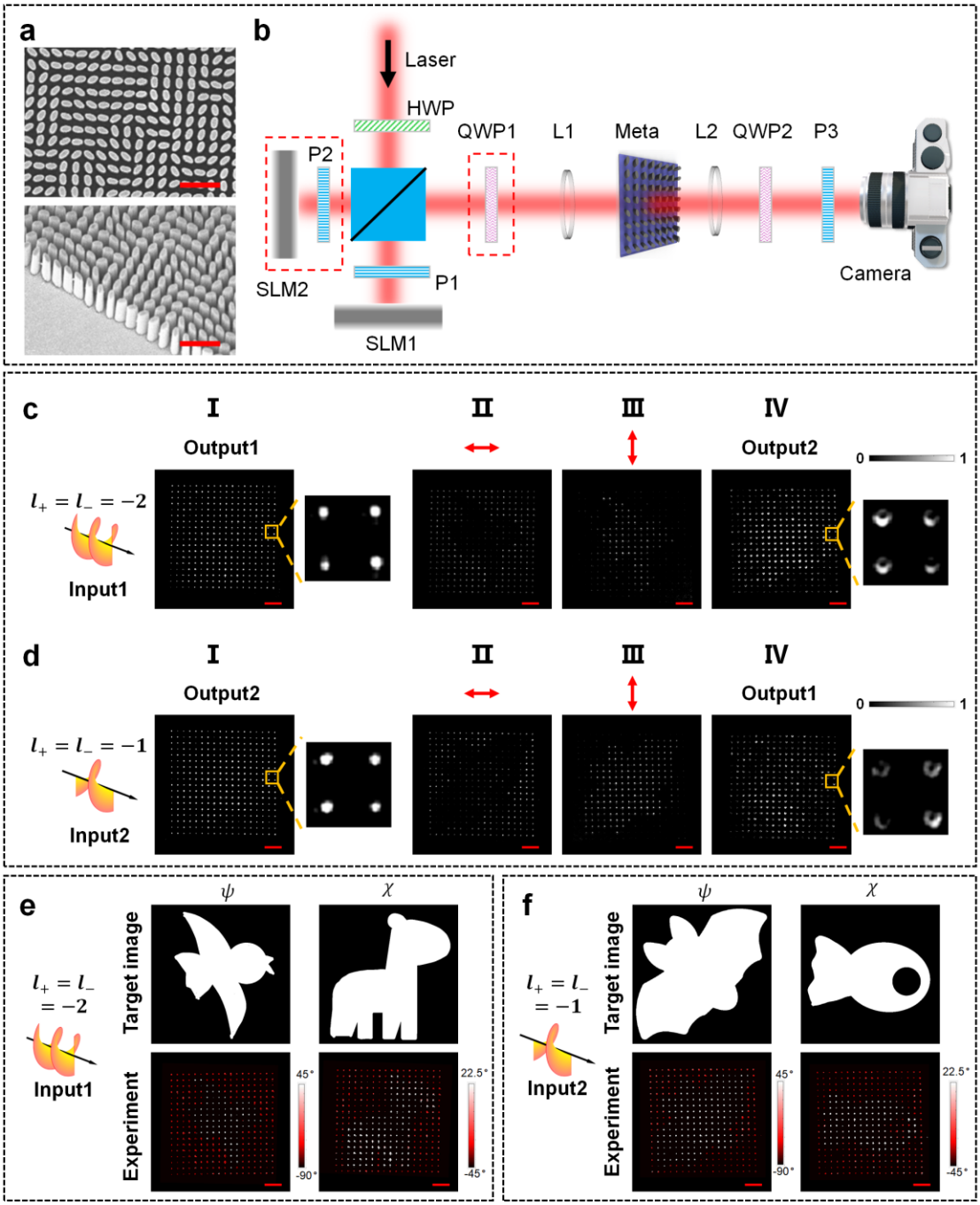

Figure 4. Experimental characterization with identical OAMs in each TAM pair channel ($l_+^i = l_-^i$). (**a**) SEM images of the fabricated metasurface under top and tilted view. Scale bar: 1μm. (**b**) Experimental setup of the holographic measurement. HWP: half wave plate; L1-L2: lens; Meta: metasurface; P1-P3: polarizers; QWP1-QWP2: quarter-wave plate; SLM1-SLM2: spatial light modulators. Components in red dashed boxes should be removed in related experiments. (**c**) Results of optical intensity distributions by illuminating a horizontally polarized vortex beam with a TC of -2. (**d**) Results of optical intensity distributions by illuminating a horizontally polarized vortex beam with a TC of -1. (**e**) Target images (top) and measured azimuth and ellipticity angle distributions (bottom) by illuminating a horizontally polarized vortex beam with a TC of -2. (**f**)

Target images (top) and measured azimuth and ellipticity angle distributions (bottom) by illuminating a horizontally polarized vortex beam with a TC of -1. Scale bar: 500 μm.

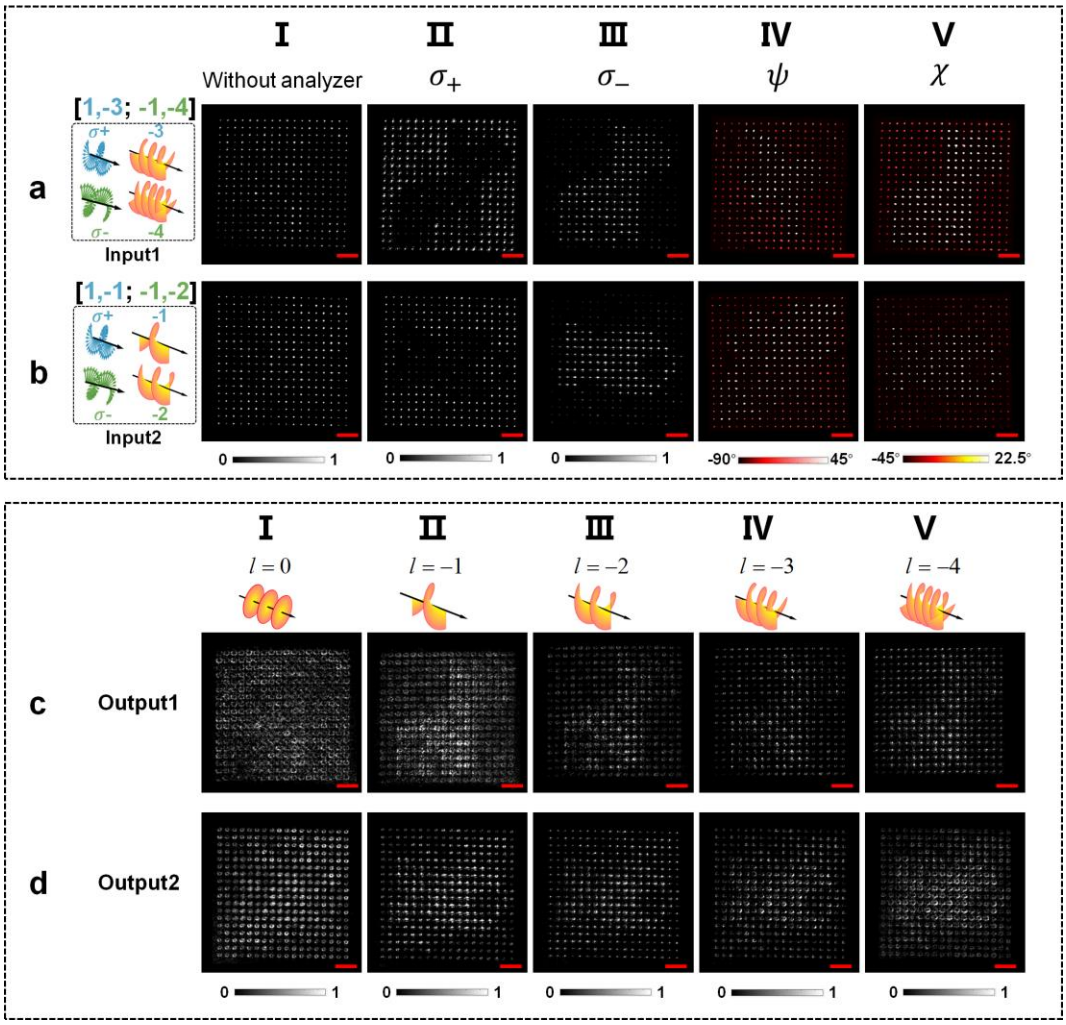

Figure 5. Experimental characterization with distinct OAMs in each TAM pair channel ($l_+^i \neq l_-^i$). (a) Measured results by illuminating a TAM pair of [1, -3; -1, -4]; (b) Measured results by illuminating a TAM pair of [1, -1; -1, -2]; (c) Results of optical intensity distributions in the region of Output1 by illuminating a horizontally polarized vortex beam with TCs ranging from 0 to -4; (d) Results of optical intensity distributions in the region of Output2 by illuminating a horizontally polarized vortex beam with TCs ranging from 0 to -4. Scale bar: 500 μm.

Spin-Orbit-Locking Vectorial Metasurface Holography

A new multi-channel vectorial holography method is introduced by using spin-orbit-locking vortex beams, which encodes TAMs with SAMs and OAMs. This approach allows for high selectivity in SAM and OAM, enabling advanced optical information processing and photonic device design.

Zhipeng Yu, Xinyue Gao, Jing Yao, Haoran Li, Yuzhi Shi, Bo Li, Zhenwei Xie, Xiaocong Yuan, Puxiang Lai,* and Qinghua Song**

ToC figure

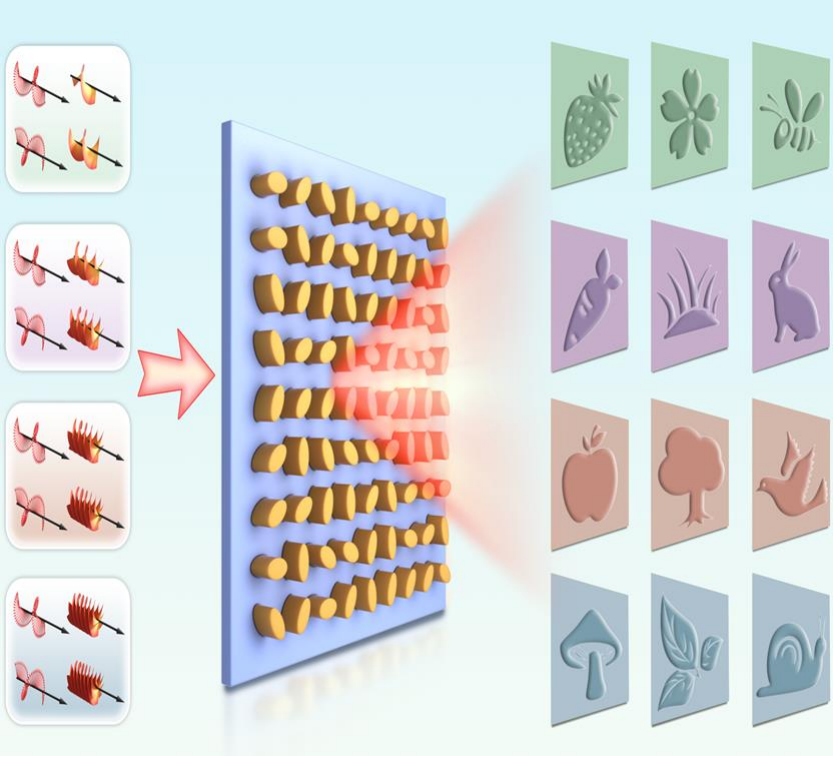

Supporting Information

Spin-Orbit-Locking Vectorial Metasurface Holography

Zhipeng Yu, Xinyue Gao, Jing Yao, Haoran Li, Yuzhi Shi, Bo Li, Zhenwei Xie, Xiaocong Yuan, Puxiang Lai,* and Qinghua Song**

Supplementary Note 1: Detailed arrangement of the vectorial fields.

Each vectorial field with a 2D point-like field distribution with desired amplitude (A), polarization azimuth (ψ) and ellipticity (χ) angle distribution is arranged at a distinct position with an equal interval.

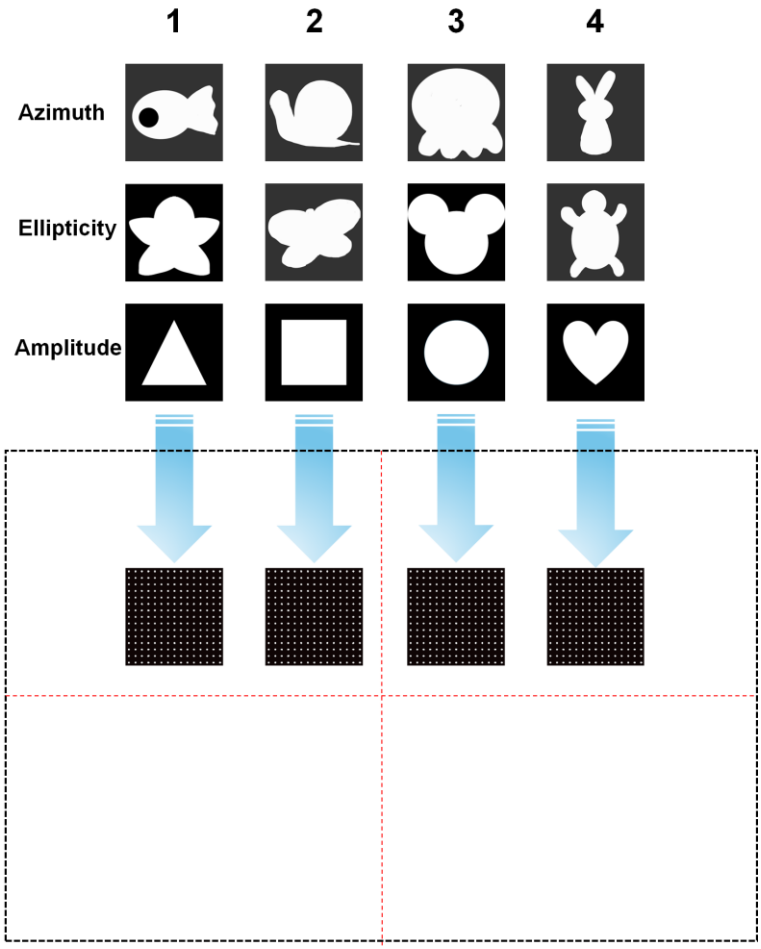

Figure S1. The arrangement of vector fields in the Fourier plane.

Supplementary Note 2: Modified Gerchberg-Saxton (GS) algorithm.

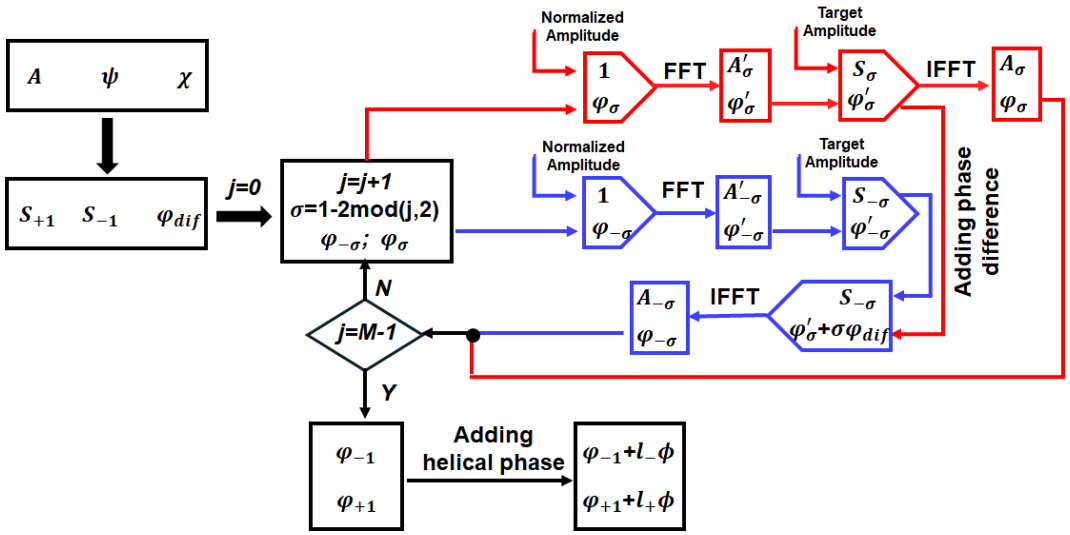

Figure S2. The flowchart of modified GS algorithm.

The modified GS algorithm flow chart for multiple OAM and polarization encryption is shown in Fig. S2. Two amplitude values (S_{+1} and S_{-1}) with opposite spin states and phase difference (φ_{dif}) between these two spin states in the Fourier plane can be calculated from a vectorial field with desired amplitude (A), azimuth angle (ψ) and ellipticity angle (χ). The initial phases with opposite spin states are randomly selected and then substituted into the algorithm for iteration. To demonstrate the process in detail, we use σ = 1 (LCP) as a reference. In a single iteration cycle, the flowchart marked in red corresponds to deriving the phase profile of the spin state for σ = 1, while the one marked in blue corresponds to σ = -1 (RCP). After performing a fast Fourier transform (FFT), the amplitudes and phases of the two spin states in the Fourier plane can be obtained. Then, the amplitudes of both spin states will be replaced with the desired amplitudes. The phase for σ = 1 is maintained, while the phase for σ = -1 will be replaced with the sum of the phase for σ = 1 and the required phase difference (φ_{dif}) between these two spin states. An inverse FFT is ultimately applied to these two optical fields to obtain the desired optical fields on the metasurface plane, with only the phases carried over to the next cycles, specifically for σ = -1. In each iteration, the processes for the two

spin states are alternated and linked by φ_{dif}, with their order determined by whether the iteration count is odd or even. Finally, two different OAM phases are added into the calculated phases for the respective spin states after the iteration process.

Supplementary Note 3: Detailed simulation results of multi-channel TAM vectorial holography.

As shown in Figs. S3(I-IV), the diagonal images, marked with green dotted boxes, exclusively exhibit point-like intensity distributions with the correct patterns for valid input-output pairs, which include, respectively, triangle, square, circle, and heart shapes. In contrast, the other images show either multiple donut-like ring structures or random superimpositions of these patterns. The polarizations of the output fields corresponding to the diagonal images will be further analyzed. Figs. S3(V) and S3(VI) display the optical intensity distributions in two opposite SAM states, which exhibit complementary patterns due to the orthogonality of these states. Furthermore, Figs. S3(VII) and S3(VIII) show the ellipticity angle distributions of a five-point star, butterfly, Mickey, and turtle, and the azimuth angle distributions of fish, snail, octopus, and rabbit in each channel, respectively.

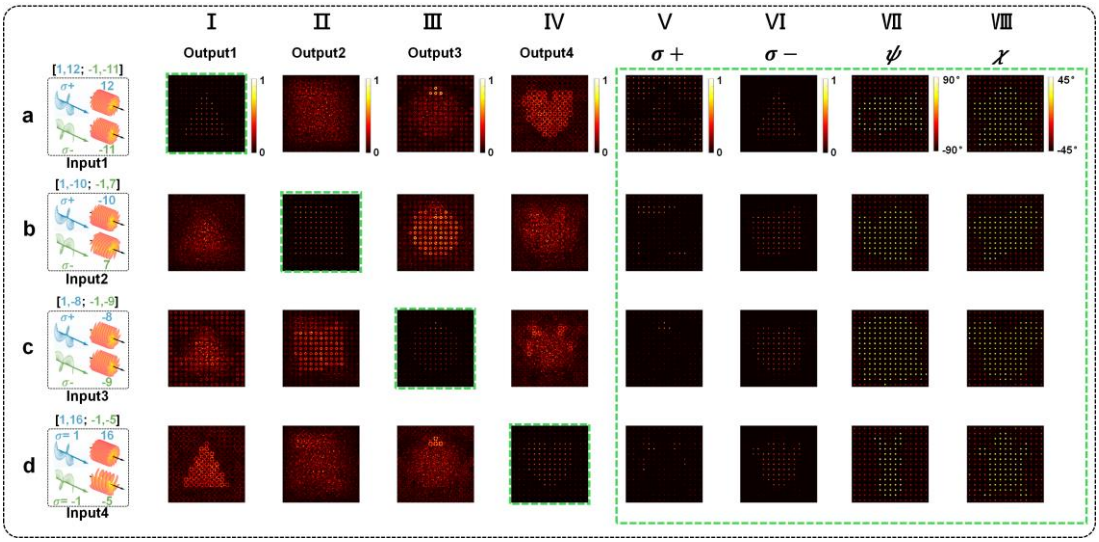

Figure S3. Numerical demonstration of the TAM vectorial metasurface holography.

Supplementary Note 4: Analysis of crosstalk in the TAM vectorial metasurface holography.

Figure S4 shows the simulated results of the full optical intensity distribution when the metasurface is illuminated by different TAM pairs. It can be observed that in the designated channels, when the correct TAM is incident, the corresponding pattern exhibits a spot array. However, crosstalk from other channels will display donut patterns instead of spot array due to the mismatch in TAM. Therefore, by placing different vectorial field channels at different spatial locations, the desired image with spot array can be clearly identified. For example, in Fig. S4a, a designed triangular pattern is displayed for the desired channel (highlighted in the dashed box), where each spot in the pattern exhibits a Gaussian beam profile. In contrast, the other channels exhibit two types of donut patterns or their superimposed patterns, which can be easily distinguished. This characteristic allows us to filter out the desired image and effectively avoid the crosstalk.

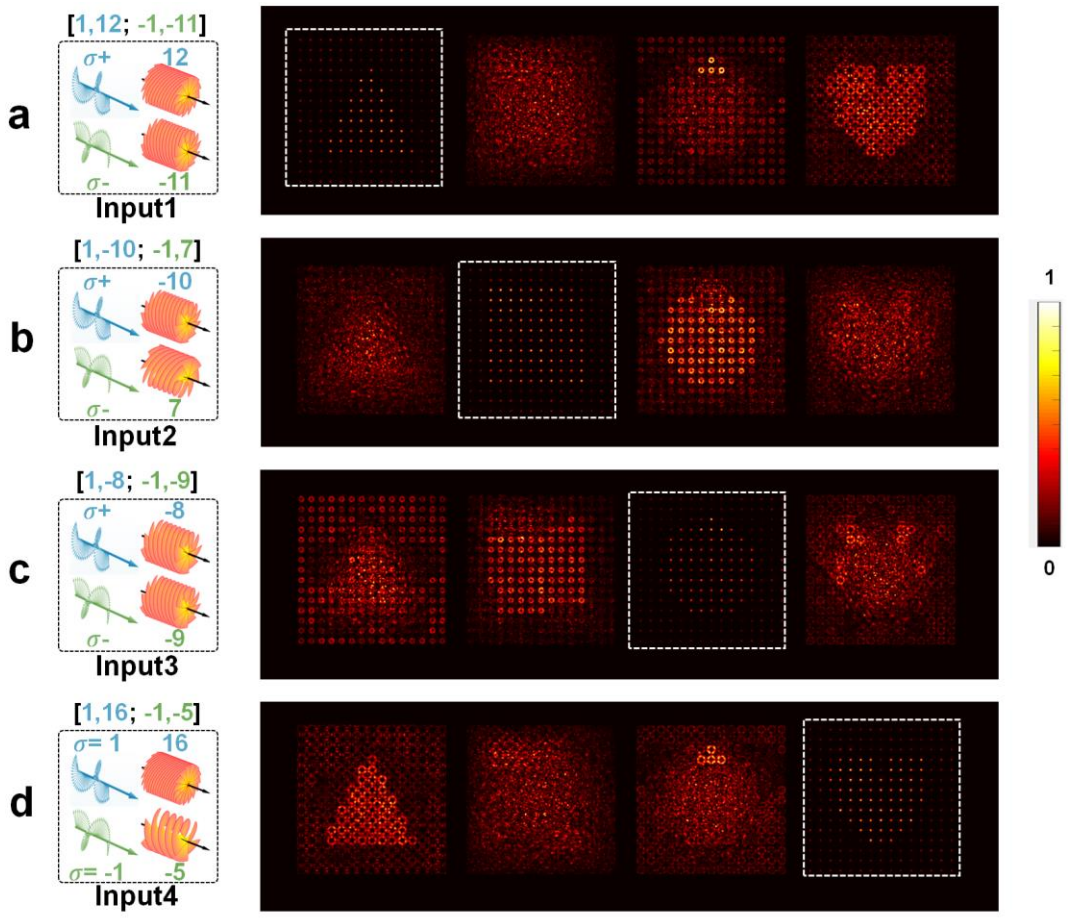

Figure S4. Analysis of crosstalk in the TAM vectorial metasurface holography.

Supplementary Note 5: Stokes parameter measurement.

In order to measure the polarization of the vectorial field accurately, an 8-step measurement is taken without removing or inserting any components during the process[1]. The optical setup of the polarization measurement is shown in Fig. S5. A quarter waveplate (QWP) with its fast axis along the x-axis and a linear polarizer (LP) with the transmission axis along the x-axis are placed before the holographic image. We need to select at least eight angles with equal intervals between 0° and 180° to measure the optical power. The measured powers at 8 different angles (shown in Table S1) can be used to calculate four Fourier coefficients (A, B, C, and D):

$$A=\frac{2}{N}\sum_{n=1}^{N}P_n;B=\frac{4}{N}\sum_{n=1}^{N}P_n\sin(2\theta_n);C=\frac{4}{N}\sum_{n=1}^{N}P_n\cos(4\theta_n);D=\frac{4}{N}\sum_{n=1}^{N}P_n\sin(4\theta_n) \quad \text{(S1)}$$

Thereafter, using these coefficients, we can calculate the Stokes parameters:

$$S_0=A-C;S_1=2C;S_2=2D;S_3=B \quad \text{(S2)}$$

The azimuth angle and ellipticity angle can be extracted from the Stokes parameter as:

$$\psi=\frac{1}{2}\tan^{-1}(S_2/S_1);\chi=\frac{1}{2}\sin^{-1}(S_3/S_0) \quad \text{(S3)}$$

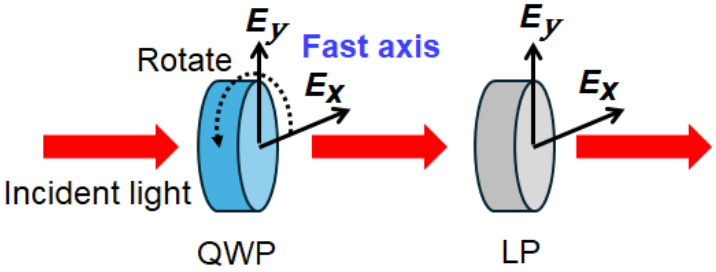

Figure S5. Optical setup of the polarization measurement. LP: linear polarizer; QWP: quarter waveplate.

n	1	2	3	4	5	6	7	8
Waveplate angle(°)	0	22.5	45	67.5	90	112.5	135	157.5
Measured power	P_1	P_2	P_3	P_4	P_5	P_6	P_7	P_8

Table S1 Eight powers at eight different rotation angles with an interval of 22.5°.

Supplementary Note 6: Experimental results of multiplexing four optical vectorial fields with each uniquely encoded with independent amplitude, polarization azimuth, and ellipticity angle.

We have also made significant advancements by experimentally designing four optical vectorial fields. Each channel is uniquely encoded with independent amplitude, polarization azimuth, and ellipticity angles, enabling the transmission of twelve capital letters from "A" to "L", as shown in Fig. S6. Scanning electron microscope (SEM) images depicting the top and perspective view of the new fabricated metasurface are presented in Fig. S6a. To present our results more clearly, we have outlined the contours of each pattern. Four optical spot arrays, each with distinct patterns labeled from "A" to "D", can be observed in the corresponding channels when the metasurface is illuminated with vortex beams (VBs) featuring topological charges (TCs) ranging from -4 to 4, as shown in Fig. S6b. Additionally, Figs. S6c and S6d display the polarization azimuth and ellipticity angle distributions of the corresponding vector fields. All patterns can be clearly observed except for the letter "I", which is primarily attributed to fabrication errors of the metasurface. In principle, the maximum number of vectorial channels is given by the formula $\frac{N^2/n^2}{2}$, where *N* and *n* are the pixel number along the width of the metasurface and each vectorial field, respectively, assuming the metasurface and all vectorial fields are square.

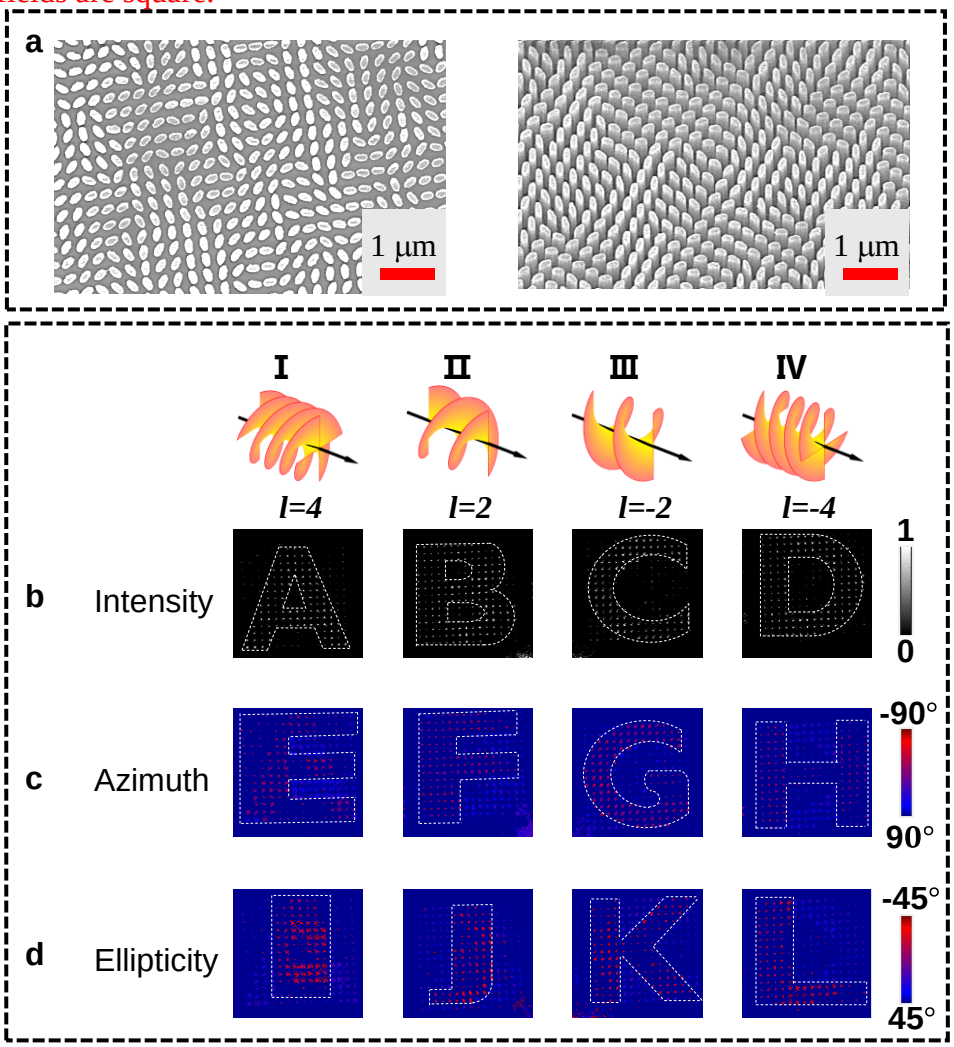

Figure S6. Experimental characterization with identical OAMs in four TAM pair channels ($l_+^i = l_-^i$). (a) SEM images of the fabricated metasurface under top and tilted view. Optical intensity distributions **(b)**, azimuth angle distributions **(c)**, and ellipticity angle

distributions **(d)** are presented for each vector field when illuminated by a horizontally polarized vortex beam. The topological charges (TCs) of the vortex beam are -4, -2, 2, and 4, respectively. The dashed line in b-d is manually added to enhance the visualization.

Supplementary Note 7: Simulation results of 3D multi-channel SOL-VMH.

To illustrate the potential of our approach for 3D vectorial holography, four channels are designed at two image planes by further adding different FT lens functions to the phase information of the holograms. To be specific, these two planes have focal lengths of 1 mm and 2 mm, respectively, with each plane featuring two channels. In Plane 1, the vector fields at Outputs 1 and 2 can only be reconstructed when the correct illumination is applied (as shown in Figs. S7a and b); similarly, in Plane 2, the vector fields at Outputs 3 and 4 can only be reconstructed under the correct illumination conditions (as depicted in Figs. S7g and h).

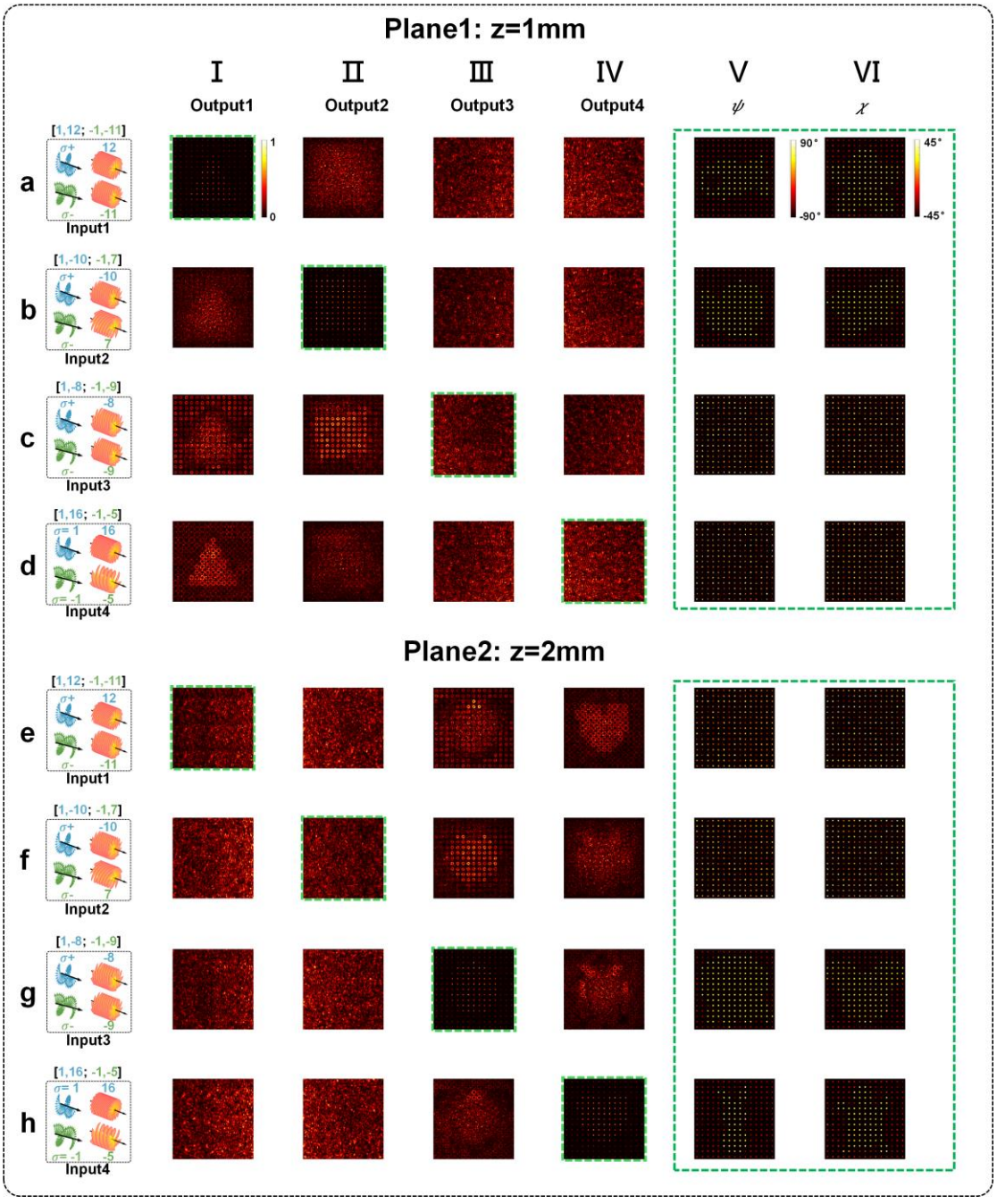

Figure S7. Numerical demonstration of the SOL-VMH in multi planes.

REFERENCES

[1] Schaefer B, Collett E, Smyth R, Barrett D, Fraher B., *American Journal of Physics* 75, 163-168 (2007).